2.5D Multi-view Averaging Diffusion Model for 3D Medical Image Translation: Application to Low-count PET Reconstruction with CT-less Attenuation Correction

Tianqi Chen^{b,d}, Jun Hou^{b,d}, Yinchi Zhou^a, Huidong Xie^a, Xiongchao Chen^a, Qiong Liu^a, Xueqi Guo^a, Menghua Xia^b, James S. Duncan^{a,b,c}, Chi Liu^{a,b}, Bo Zhou^{a,e}

^aDepartment of Biomedical Engineering, Yale University, New Haven, CT, USA
 ^bDepartment of Radiology and Biomedical Imaging, Yale School of Medicine, New Haven, CT, USA
 ^cDepartment of Electrical Engineering, Yale University, New Haven, CT, USA.
 ^dDepartment of Computer Science, University of California Irvine, Irvine, CA, USA
 ^eDepartment of Radiology, Northwestern University, Chicago, IL, USA.

Abstract

Positron Emission Tomography (PET) is an important clinical imaging tool but inevitably introduces radiation hazards to patients and healthcare providers. Reducing the tracer injection dose and eliminating the CT acquisition for attenuation correction can reduce the overall radiation dose, but often results in PET with high noise and bias. Thus, it is desirable to develop 3D methods to translate the non-attenuation-corrected low-dose PET (NAC-LDPET) into attenuation-corrected standard-dose PET (AC-SDPET). Recently, diffusion models have emerged as a new state-of-the-art deep learning method for image-to-image translation, better than traditional CNN-based methods. However, due to the high computation cost and memory burden, it is largely limited to 2D applications. To address these challenges, we developed a novel 2.5D Multi-view Averaging Diffusion Model (MADM) for 3D image-to-image translation with application on NAC-LDPET to AC-SDPET translation. Specifically, MADM employs separate diffusion models for axial, coronal, and sagittal views, whose outputs are averaged in each sampling step to ensure the 3D generation quality from multiple views. To accelerate the 3D sampling process, we also proposed a strategy to use the CNN-based 3D generation as a prior for the diffusion model. Our experimental results on human patient studies suggested that MADM can generate high-quality 3D translation images, outperforming previous CNN-based and Diffusion-based baseline methods.

Keywords: Low-count PET, Attenuation Correction, Denoising, Diffusion Model, 3D Image Translation

1. Introduction

Positron emission tomography (PET) is a vital functional imaging tool with wide applications in oncology, cardiology, neurology, and biomedical research. In clinical practice, PET imaging involves radioactive tracer injection to the patients, with the dosage level carefully able (ALARA) Strauss and Kaste (2006). In order to correct the attenuation of the PET signal, PET is also acquired along with CT to provide an attenuation map (μ -map) for PET attenuation correction (AC). This multimodal imaging procedure inevitably introduces radiation hazards to the patient and healthcare providers. Thus, it is highly desirable to reduce the overall radiation dose in this important imaging procedure. On one hand, the PET radiation dose can be directly reduced by reducing

guided by the principle of As Low As Reasonably Achiev-

^{*}Corresponding author.

Email address: bo.zhou@northwestern.edu (Bo Zhou)

the tracer injection dose. However, the PET image will suffer from high noise and bias with the low-count signal. On the other hand, while PET can be acquired alone without CT, the PET image would inevitably suffer further increased quantification errors if CT-based AC is not included. Thus, reconstruction of standard-count PET from low-count PET and CT-less AC for PET are both important topics for reducing the overall radiation dose in PET imaging, as illustrated in Figure 1.

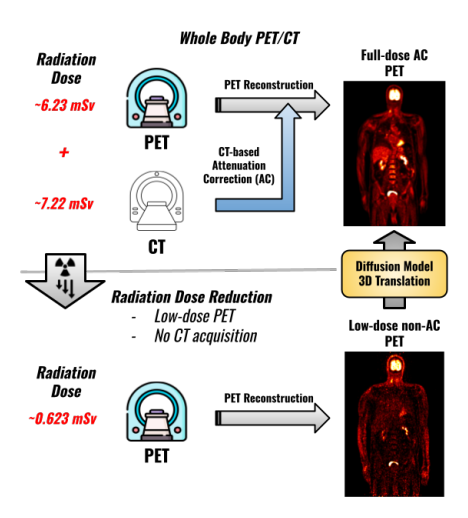


Figure 1: Illustration of low-count/dose PET reconstruction with CT-less Attenuation Correction (AC) for reducing the overall radiation dose in PET.

There are many previous works on low-count PET image denoising, and can be summarized into two categories, including conventional image post-processing Dutta et al. (2013); Maggioni et al. (2012); Mejia et al. (2016) and deep learning (DL) based methods Xiang et al. (2017); Wang et al. (2018); Lu et al. (2019); Kaplan and Zhu (2019); Hu et al. (2020); Gong et al. (2020); Zhou et al. (2020); Ouyang et al. (2019); Chen et al. (2019); Liu et al. (2020a); Xie et al. (2023); Pan et al. (2024). Conventional image post-processing techniques, such as Gaussian filtering, are standard techniques in PET reconstruction but hard to preserve local structures. Nonlocal mean filter Dutta et al. (2013) and block-matching 4D filter Maggioni et al. (2012) were proposed to denoise low-dose PET while better preserving the structural information. While these conventional image postprocessing methods may substantially improve the image quality, over-smoothing is commonly observed in ultralow-count settings. As the statistical characteristics of noise in medical imaging are complex and hard to model, DL models can learn the highly non-linear relationship from data and recover the original signal from noise. Previous DL-based methods can be further divided into two categories. The first category only uses the low-count PET data as input. For example, Kaplan et al. Kaplan and Zhu (2019) proposed using a GAN Goodfellow et al. (2014) with UNet Ronneberger et al. (2015a) as the generator to predict standard-count PET from low-count PET. Similarly, Wang et al. Wang et al. (2018) proposed using a 3D-conditional-GAN Isola et al. (2017a) also with UNet as the generator to translate low-count PET to standardcount PET. Zhou et al. Zhou et al. (2020) and Gong et al. Gong et al. (2020) found incorporating Wasserstein GAN Arjovsky et al. (2017) can also achieve promising lowcount PET denoising performance. The second category uses low-count PET and MR/CT as input. For example, Xiang et al. Xiang et al. (2017) proposed a deep autocontext CNN that takes low-count PET image and T1 MR image as input for prediction of standard-count PET. Similarly, Chen et al. (2019) proposed to input low-count PET along with multi-contrast MR images into a UNet Ronneberger et al. (2015a) for ultra-low-dose PET denoising. Compared to conventional PET denoising methods, all these DL-based methods achieved superior denoising performance. However, almost all of these previous methods were developed based on U-Net or its variantsRonneberger et al. (2015a); Isola et al. (2017a); Zhu et al. (2017). Most importantly, they assumed CT-based AC is already done for the low-count PET, thus CT-less AC for further reducing the radiation was not considered.

On the other hand, there are also many previous efforts for CT-less AC for PET. For time-of-flight (TOF) PET imaging data, Maximum Likelihood Reconstruction of Activity and Attenuation (MLAA) algorithms Rezaei et al. (2016) were first developed to simultaneously reconstruct the tracer activity (λ -MLAA) and the attenuation map (μ -MLAA), based on the TOF PET raw data only. Ideally, MLAA would solve the AC problem for TOF PET. However, the direct use of μ -MLAA still suffers from significant quantification error as compared to the CT-based (μ -CT) OSEM reconstruction Rezaei et al. (2016); Shi et al. (2023); Nuyts et al. (2018), even in the

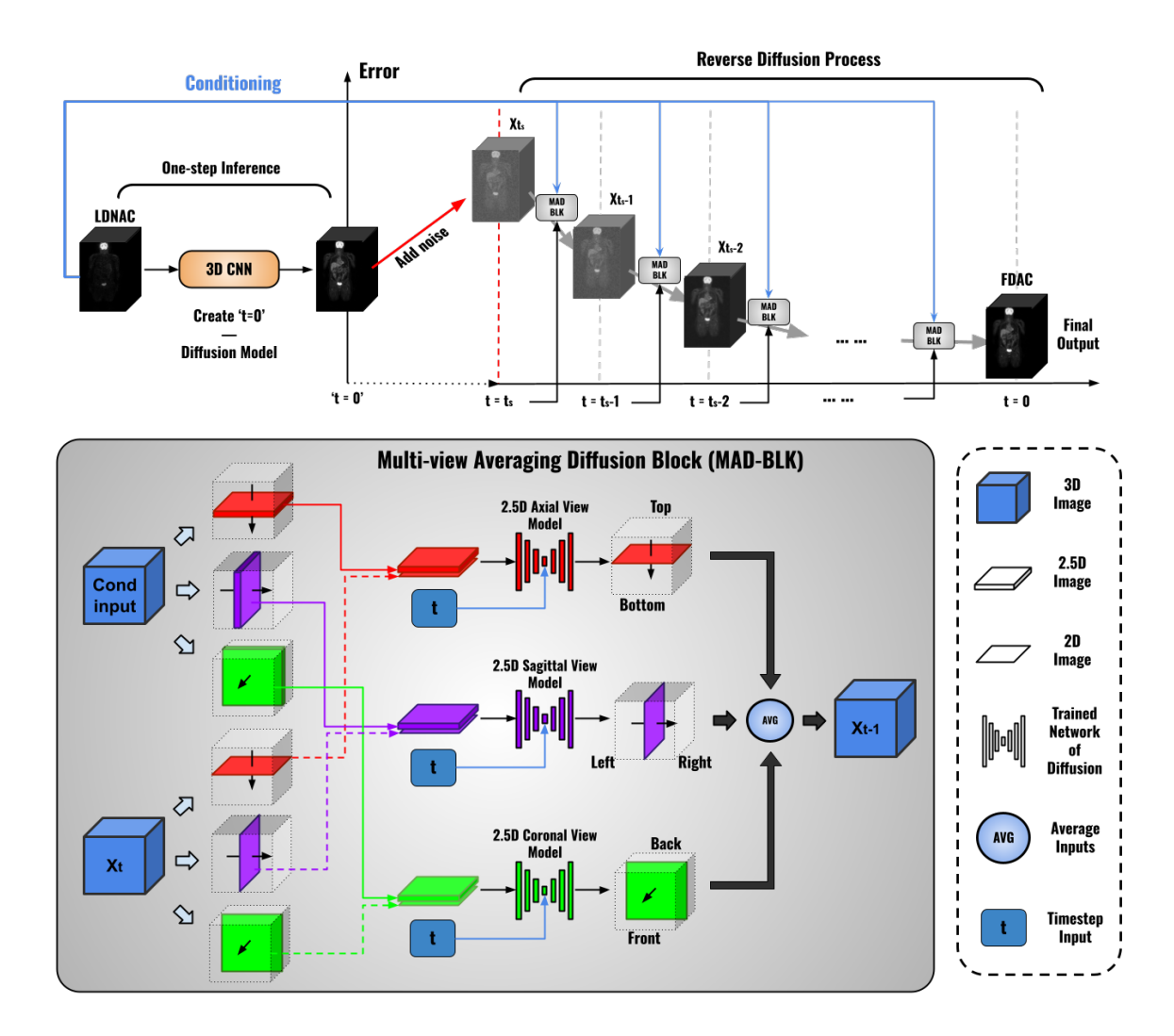


Figure 2: The overall workflow of 2.5D Multi-view Averaging Diffusion Model (MADM). MADM contains a one-step inference generative model(orange) and MAD-BLK(grey). The MAD-BLK contains Three models in axial, sagittal, and coronal view, and the output of each model will be averaged in the average block before output.

standard-count PET. With recent advancements in deep learning (DL), DL-based CT-less AC methods have been extensively investigated to address this challenge Lee (2020); Chen and Liu (2023). The previous DL-based AC methods can be summarized into two classes. The first category of methods uses either non-attenuation corrected (NAC) PET or MLAA reconstructions as deep network input to generate CT-based μ -map Shi et al. (2023);

Toyonaga et al. (2022); Liu et al. (2018a,b); Hwang et al. (2019); Dong et al. (2019). Then, AC is performed based on the generated μ -map. Similarly, the second category of methods also uses either NAC PET or MLAA reconstructions as deep network input, but to directly generate attenuation-corrected PET Shiri et al. (2019); Dong et al. (2020); Shiri et al. (2023). However, almost all of these previous methods were developed based on U-Net or its

```
Input: x \in N^{d_1 \times d_2 \times d_3}
Initialize #1: t_s \in [0,T]: the start timestep of denoising process
Initialize #2: s: the number of adjacent slices loaded as 2.5D condition input
Initialize #3: \epsilon \sim N(0,I)

y_{\text{prior}} = f_{\text{prior}}(x); \Rightarrow One-step inference to generate prior image
\bar{y}_{\text{prior}} = \sqrt{a_{t_0}} y_{\text{prior}} + \sqrt{1-\bar{a}_{t_0}} \epsilon; \Rightarrow Diffuse, i.e. add noise, to the prior image
for t = t_s, t_s - 1, ..., 0 do
 \begin{vmatrix} y_t^{\text{avg}} = \bar{y}_{\text{prior}} & \text{if } t = t_s \\ y_t^{\text{avg}} = \bar{y}_{\text{prior}} & \text{if } t = t_s \\ z \sim N(0,T) & \text{if } t > 1, \text{ clse } z = 0 \\ \text{for } i = 1, 2, ..., d_1 & \text{do} \\ y_{t-1}^{\text{co}}[i, :, :] = \frac{1}{\sqrt{a_t}} (y_t^{\text{avg}}[i, :, :] - \frac{1-\alpha_t}{\sqrt{1-\bar{a_t}}} f_t^{\text{co}}(y_t^{\text{avg}}[i, :, :], x[i-s:i+s, :], t)) + \sigma_t z; \Rightarrow \text{Coronal view 2.5D} \\ \text{reverse} \\ \text{for } i = 1, 2, ..., d_2 & \text{do} \\ y_{t-1}^{\text{sa}}[i, :, :] = \frac{1}{\sqrt{a_t}} (y_t^{\text{avg}}[:, i, :] - \frac{1-\alpha_t}{\sqrt{1-\bar{a_t}}} f_t^{\text{sa}}(y_t^{\text{avg}}[:, i, :], x[:, i-s:i+s, :], t)) + \sigma_t z; \Rightarrow \text{Sagittal view} \\ 2.5 \text{D reverse} \\ \text{for } i = 1, 2, ..., d_3 & \text{do} \\ y_{t-1}^{\text{ax}}[:, :, i] = \frac{1}{\sqrt{a_t}} (y_t^{\text{avg}}[:, :, i] - \frac{1-\alpha_t}{\sqrt{1-\bar{a_t}}} f_t^{\text{ax}}(y_t^{\text{avg}}[:, :, i], x[:, :, i-s:i+s], t)) + \sigma_t z; \Rightarrow \text{Axial view 2.5D} \\ \text{reverse} \\ \text{for } i = 1, 2, ..., d_3 & \text{do} \\ y_{t-1}^{\text{ax}}[:, :, i] = \frac{1}{\sqrt{a_t}} (y_t^{\text{avg}}[:, :, i] - \frac{1-\alpha_t}{\sqrt{1-\bar{a_t}}} f_t^{\text{ax}}(y_t^{\text{avg}}[:, :, i], x[:, :, i-s:i+s], t)) + \sigma_t z; \Rightarrow \text{Axial view 2.5D} \\ \text{reverse} \\ \text{for } i = 1, 2, ..., d_3 & \text{do} \\ y_{t-1}^{\text{ax}}[:, :, i] = \frac{1}{\sqrt{a_t}} (y_t^{\text{avg}}[:, :, i] - \frac{1-\alpha_t}{\sqrt{1-\bar{a_t}}} f_t^{\text{ax}}(y_t^{\text{avg}}[:, :, i], x[:, :, i-s:i+s], t)) + \sigma_t z; \Rightarrow \text{Axial view 2.5D} \\ \text{reverse} \\ \text{reverse} \\ \text{substitution of the prior image} \\ \text{for } i = 1, 2, ..., i = 1, i =
```

variantsRonneberger et al. (2015a); Isola et al. (2017a); Zhu et al. (2017) and only validated on standard-count PET. Even though these approaches achieved reasonable AC performance on standard-count PET, directly deploying these methods for low-count PET AC may result in non-ideal performance given the low-quality PET input. Additional steps for low-count PET denoising also need to be considered even after AC is performed.

While reconstruction of standard-count PET from low-count PET task and CT-less AC for standard-count PET task were both extensively studied in prior works, low-count PET reconstruction with CT-less AC that can holistically reduce radiation dose has not been investigated before. Directly deploying previous DL models may lead to non-ideal translation results since the low-count PET image without AC not only suffers from high noise levels but also significant bias due to attenuation. In recent years, the Diffusion Model (DM) has emerged as the new state-of-the-art image generation method and has shown promising results in image-to-image translation. However, there are two major issues with DM. First, these

methods were mainly developed for 2D image data, but not 3D data like PET. Translating 3D images in a slice-by-slice 2D manner will lead to inconsistency from another view Xie et al. (2023); Lee et al. (2023); Chung et al. (2023). Even though it is possible to directly extend the 2D network into the 3D network in the diffusion model for 3D translation, the computation burden and memory requirement make it highly infeasible with the current hardware technique, especially when it is applied to high-resolution 3D imaging data like PET. Second, the translation speed is significantly slower than previous CNN-based approaches, due to the large number of diffusion sampling steps required. This is further exacerbated if DM is directly extended to 3D imaging data like PET.

To address these issues, we developed a novel 2.5D Multi-view Averaging Diffusion Model (MADM) for 3D medical image translation with the first application on low-count PET reconstruction with CT-less AC. There are three main contributions of MADM. First, to reduce the computational demands associated with 3D models and

to mitigate the discontinuities inherent in 2D models, we proposed to use a 2.5D model that incorporates several adjacent slices in addition to the target slice for prediction. Second, to further minimize discontinuities and enhance prediction accuracy, we proposed to train separate 2.5D models for each view in 3D, i.e. axial, coronal, and sagittal views. During the inference, we average the result in each denoising step of the diffusion process. Third, to expedite the translation process and refine generated image accuracy, we proposed to utilize 3D predictions from a Convolutional Neural Network (CNN)-based model as a prior for our diffusion model. Our experimental results show that MADM can generate high-quality AC standardcount PET(AC-SDPET) directly from the NAC low-count PET(NAC-LDPET) in 3D with reasonable computation resources, and also surpassing several previous baselines.

2. Methods

2.1. Cascaded Multi-path Shortcut Diffusion Model

The general pipeline of the 2.5D Multi-view Averaging Diffusion Model (MADM) is depicted in Figure 2. During both training and sampling processes, MADM employs a multifaceted approach: first, we use a CNN-based one-step inference generative model to create a 3D prior image, then we use multiple conditional 2.5D diffusion models in axial, coronal, and sagittal view and average the outputs from different views in each denoising step to further refine the 3D prior image. The following section details the training and inference methodologies.

2.2. 2.5D Multi-view Averaging Diffusion

We denote the NAC-LDPET input image as $x \in N^{d_1 \times d_2 \times d_3}$ and the target AC-SDPET image as $y \in N^{d_1 \times d_2 \times d_3}$ where d_1, d_2, d_3 is the width, depth, and hight of the 3D image.

Training: To generate the prior image for MADM, we first need to train a one-step inference generative model $f_{\text{prior}}(\cdot)$, i.e. U-Net Ronneberger et al. (2015a) here, which predicts y_0 from x. This model can be trained using the L2 loss

$$\mathcal{L}_{v} = ||f_{\text{prior}}(x) - y||_{2}^{2}, \tag{1}$$

On the other hand, the diffusion process tries to predict the distribution $y_0 \sim q(y)$. Then we have a forward

diffusion process which adds noise ϵ to y_0 for T steps:

$$q(y_t|y_{t-1}) = \mathcal{N}(y_t; \sqrt{1-\beta_t}y_{t-1}, \beta_t I),$$
 (2)

and

$$q(y_{1:T}|y_0) = \prod_{t=1}^{T} q(y_t|y_{t-1}),$$
 (3)

where we let $\beta_t \in (0, 1)_{t=1}^T$ and $\beta_t < \beta_{t+1}$. Following that, we can sample y_t for any $t \in [0, T]$ using:

$$y_t = \sqrt{\bar{\alpha}_t} y_0 + \sqrt{1 - \bar{\alpha}_t} \epsilon, \tag{4}$$

$$q(y_t|y_0) = \mathcal{N}(y_t; \sqrt{\bar{\alpha}_t}y_0, (1 - \bar{\alpha}_t)I), \tag{5}$$

where $\epsilon \sim N(0, I)$, $\alpha_t = 1 - \beta_t$, and $\bar{\alpha}_t = \prod_{i=1}^t \alpha_i$. Then in the reverse diffusion process(denoising process), we want to sample y_0 from $y_T \sim \mathcal{N}(0, I)$, thus we need a model p_θ to run this reverse diffusion process which

$$p_{\theta}(y_{t-1}|y_t) = \mathcal{N}(y_{t-1}; \mu_{\theta}(y_t, x, t), \beta_t I),$$
 (6)

and

$$p_{\theta}(y_{0:T}) = p(y_T) \prod_{t=1}^{T} p_{\theta}(y_{t-1}|y_t), \tag{7}$$

where

$$\mu_{\theta}(y_t, x, t) = \frac{1}{\sqrt{\alpha_t}} (y_t - \frac{1 - \alpha_t}{\sqrt{1 - \bar{\alpha}_t}} f_{\theta}(y_t, x, t)), \quad (8)$$

Therefore we can use model $f_{\theta}(\cdot)$ to predict y_{t-1} from y_t given the NAC-LDPET input x. In our MADM, instead of using a whole 3D x as the conditional input, we use 2.5D slices x^v cropped (2s + 1) adjacent slices from x in different views $v \in \{\text{coronal}, \text{sagittal}, \text{axial}\}$.

To train the conditional diffusion model $f_{\theta}^{v}(\cdot)$ separately in coronal, sagittal, and axial view, we use pixel-wise L2 loss

$$\mathcal{L}_{v} = \|f_{\theta}^{v}(y_{t}^{v}, x^{v}, t) - \epsilon\|_{2}^{2}, \tag{9}$$

where t = 0, 1, ..., T is the timestep in diffusion process.

Sampling: After the loss of conditional diffusion models f_{θ}^{v} and f_{prior} converged in training, we use f_{prior} to predict the y_{prior} from x

$$y_{\text{prior}} = f_{\text{prior}}(x).$$
 (10)

Then we add noise to the y_{prior} to the same noise level t_s in diffusion process by

$$\bar{y}_{\text{prior}} = \sqrt{\bar{a}_{t_s}} y_{\text{prior}} + \sqrt{1 - \bar{a}_{t_s}} \epsilon,$$
 (11)

where $t_s \in [0, T]$. Following the DDPM process, the noisy image in t - 1 for the step t can be predicted using the conditional diffusion models

$$y_{t-1}^{V} = \frac{1}{\sqrt{\alpha_t}} (y_t^{V} - \frac{1 - \alpha_t}{\sqrt{1 - \bar{\alpha_t}}} f_{\theta}^{V}(y_t^{V}, x^{V}, t)) + \sigma_t z, \qquad (12)$$

where $y_{t_s} = \bar{y}_{prior}$ when $t = t_s$. After predicting the y_{t-1}^{ν} in three views, our method averages the three predictions using

$$y_{t-1}^{\text{avg}} = \frac{y_{t-1}^{\text{co}} + y_{t-1}^{\text{ax}} + y_{t-1}^{\text{sa}}}{3},$$
 (13)

to get the final prediction for step t-1 then repeat the denoise process using equation 12 and 13 from step t_s to 0 to get the final result $y_0 = y_0^{avg}$. The algorithm is summarized in Algorithm 1.

2.3. Data Preparation and Implementation Details

We collected a real patient dataset from the Yale New Haven Hospital (YNHH) for training and evaluation of our method. The data was acquired using a Siemens Biograph mCT scanner at YNHH. PET scans were performed approximately 60 mins after intravenous injection of about 10 mCi ¹⁸F-FDG tracer, with whole-body continuous bed scanning protocol. We used uniform downsampling of the PET list-mode data with down-sampling ratios of 5% and 10% to generate low-count PET data at two different low-count levels. To generate the non-AC low-count PET image (i.e. NAC-LDPET), we used the down-sampled PET list-mode data and performed reconstruction using the ordered-subsets expectation maximization (OSEM) algorithm with 2 iterations and 21 subsets without AC. On the other hand, to generate the AC full-count PET image (i.e. AC-SDPET), we used the original PET list-mode data without down-sampling and performed the same OSEM protocol but with AC. For both reconstructions, a post-reconstruction Gaussian filter with 5mm full width at half maximum (FWHM) was used. The voxel size of the reconstructed image was $4.08 \times 4.08 \times 4.06$ mm³. The image size was 200×200 in the transverse plane and varied in the axial direction depending on the patient's height. The 147 subjects were split into 120 subjects for training and 27 subjects for evaluation. We trained and implemented all models on the NVIDIA H100 GPUs. We trained our MADM model with a batch size of 50 for 200K training step with the $lr = 1 \times 10^{-4}$ and linearly decrease to 0. We used the EMA rate of 0.9999. We used the linear schedule of 1000 time steps.

2.4. Evaluation Strategies and Baselines

Using the AC-SDPET as the reference, we evaluated the 3D translation performance both quantitatively and qualitatively. First, the quality of the translated images was evaluated at the image level using three imagequality metrics, including Peak Signal-to-Noise Ratio (PSNR), Structural Similarity Index (SSIM), and Root Mean Square Error (RMSE). SSIM focuses on the evaluation of structural recovery, while RMSE with a unit of SUV and PSNR with a unit of dB stress the evaluation of intensity profile recovery. Second, the quality of the translated PET was evaluated at clinically important local lesion regions throughout the whole body. Specifically, the difference in tumors' SUV mean was analyzed. For comparative evaluation, we compared our results against previous state-of-the-art DL-based image translation methods, including UNet-based methods Ronneberger et al. (2015a), GAN-based methods Isola et al. (2017a), and Diffusion-based methods Lee et al. (2023); Bieder et al. (2023). For both quantitative and qualitative evaluations, we evaluated the performance under two different ultralow-dose/count settings, i.e. 10% and 5% of PET full counts.

3. Experimental Results

In Figure 3, we show the qualitative comparison between our method and previous state-of-the-art methods for a patient example under the 5% low-count PET scenario. As we can see, the original NAC-LDPET not only suffers from high noise levels but also highly biased quantification errors due to the attenuation effect, thus resulting in a low PSNR of 28.531 dB. The error map computing the difference between it and the AC-SDPET, i.e. ground truth, further demonstrates this issue. Using previous CNN methods, i.e. UNet Ronneberger et al. (2015b) and GAN Isola et al. (2017a), we can see that these methods can generate reasonable AC-SDPET with PSNR reach to 36.73 dB. However, relatively high errors were found in the liver and rib regions. On the other hand, we can see that previous diffusion methods, i.e. 3D-DDPM Bieder

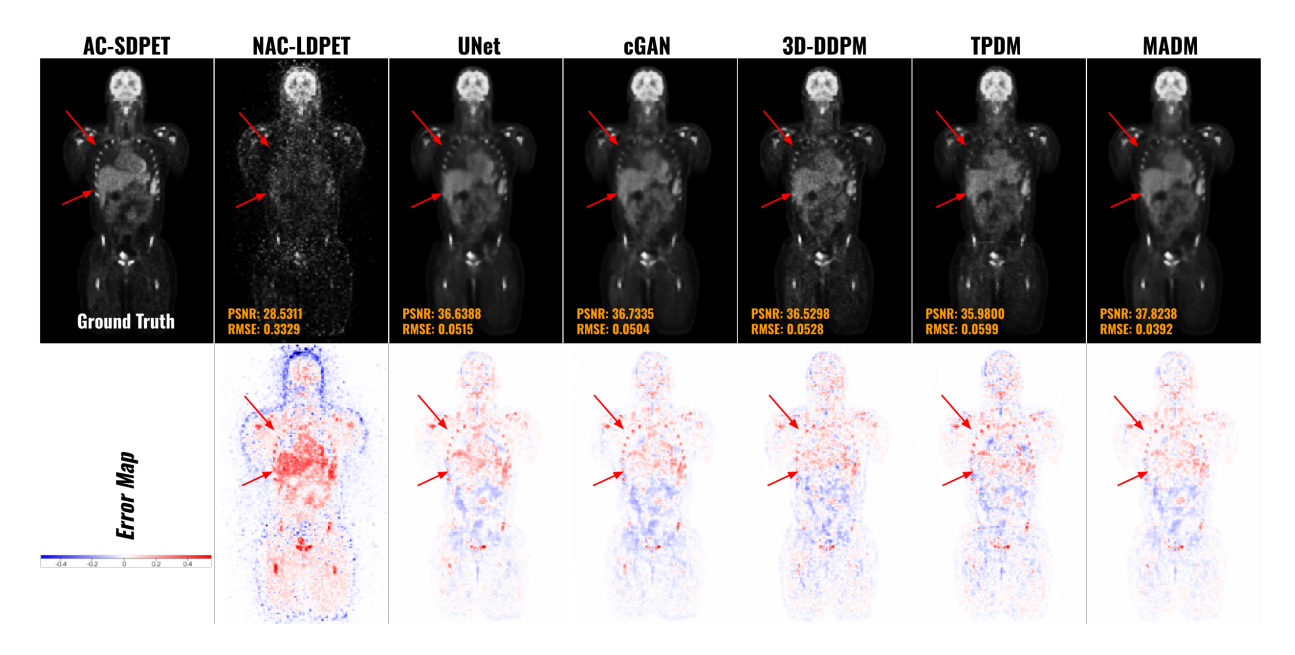


Figure 3: Visual comparison of AC-SDPET generation from different methods under 5% NAC-LDPET settings. The coronal view image(top) and error map(bottom) are shown. RMSE and PSNR values are calculated for each individual volume. The CT-based AC-SDPET(top) and image index in to the color map of the error map(bottom) are shown in the first column.

Table 1: Quantitative comparison of AC-SDPET generation from different methods under two different low-count settings using PSNR, SSIM, and RMSE. Best results are marked in **bold**.

Evaluation	5% Low-count			10% Low-count			GPU Memory Usage	
	PSNR	SSIM	RMSE	PSNR	SSIM	RMSE	Training(MB)	Sampling(MB)
NAC-LD	29.385 ± 1.440	0.9489 ± 0.0147	0.2666 ± 0.0621	30.049 ± 1.442	0.9544 ± 0.0133	0.2293 ± 0.0561	-	-
UNetRonneberger et al. (2015b)	38.101 ± 1.423	0.9936 ± 0.0021	0.0360 ± 0.0096	38.869 ± 1.384	0.9946 ± 0.0018	0.0301 ± 0.0082	10014	10460
cGANIsola et al. (2017b)	38.295 ± 1.467	0.9938 ± 0.0021	0.0344 ± 0.0087	39.045 ± 1.454	0.9948 ± 0.0018	0.0289 ± 0.0076	11440	13020
3D-DDPMBieder et al. (2023)	37.197 ± 1.271	0.9924 ± 0.0026	0.0437 ± 0.0085	37.541 ± 1.189	0.9930 ± 0.0022	0.0403 ± 0.0079	68874	23798
TPDMLee et al. (2023)	36.818 ± 1.461	0.9916 ± 0.0029	0.0485 ± 0.0150	37.463 ± 1.478	0.9925 ± 0.0027	0.0419 ± 0.0137	6442	3012
MADM	38.920 ± 1.503	0.9944 ± 0.0020	0.0299 ± 0.0088	39.453 ± 1.487	0.9952 ± 0.0017	0.0265 ± 0.0083	6442	4464

et al. (2023) and TPDMLee et al. (2023), can also generate reasonable AC-SDPET from NAC-LDPET. However, the performance in terms of PSNR and RMSE is slightly lower than the CNN-based methods. In the right column, our MADM that uses the CNN-based method's generation as prior and further refined using a multi-view 2.5D diffusion model generates the most consistent AC-SDPET as compared to ground truth, with further reduced error in major organs, e.g. liver and bone.

In Figure 4, we present another example of AC-SDPET generated from 10% low-count PET, comparing our method with previous methods. This example focuses on the tumor regions, which are zoomed in and

highlighted with an orange arrow in Figure 4. Compared to other CNN-based and diffusion-based methods, our MADM not only achieves higher PSNR and lower NMSE quantitatively, but also shows a smaller error in the tumor region, as evidenced by the error map. Although both state-of-the-art methods and our MADM exhibit larger errors in the tumor region, our MADM significantly reduces errors in the surrounding areas. This reduction in error provides a substantial benefit for lesion masking and further analysis.

The quantitative comparisons were summarized in Table 1. Similar to the observations from the visualizations, we can see that the traditional CNN-based approaches can

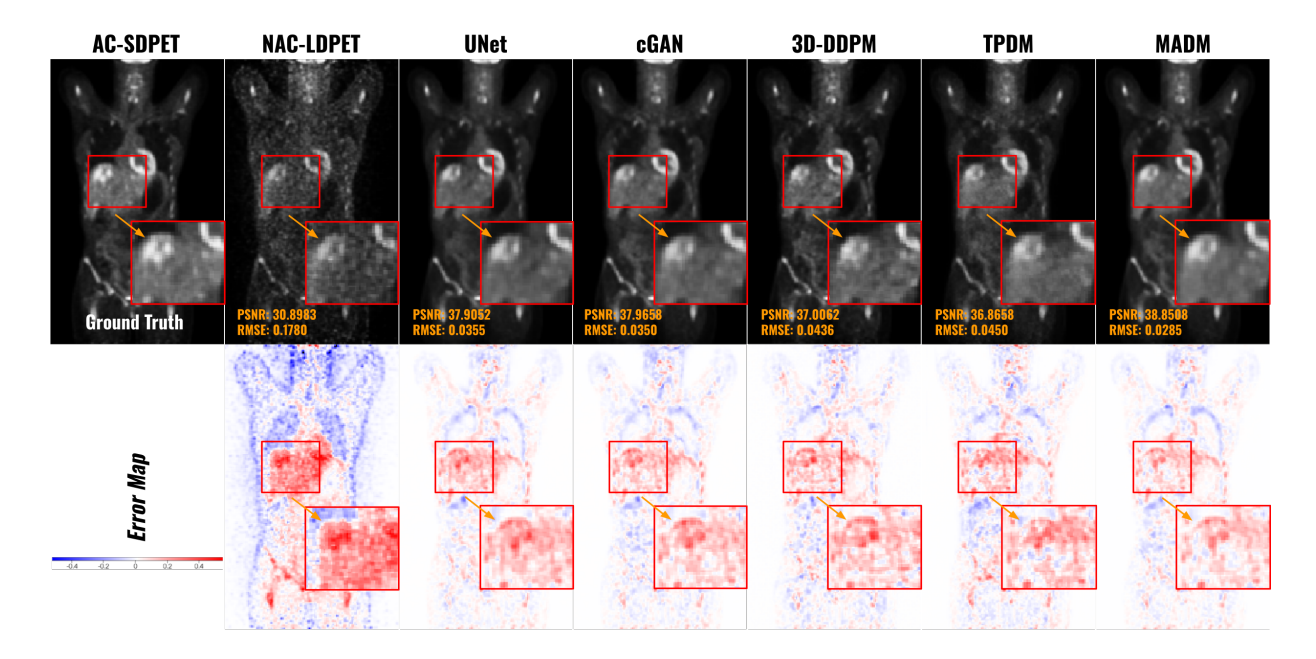


Figure 4: Visual comparison of AC-SDPET generation from different methods under 10% NAC-LDPET settings. The coronal view image(top) and error map(bottom) are shown. RMSE and PSNR values are calculated for each individual volume. The CT-based AC-SDPET(top) and image index in to the color map of the error map(bottom) are shown in the first column.

slightly outperform the diffusion-based approach in our 3D scenario. For example, the cGANIsola et al. (2017b) achieved the best performance among all the baselines with PSNR = 38.295 dB under the 5% low-count scenario, while the best previous diffusion method, i.e. 3D-DDPMBieder et al. (2023), only achieved PSNR = 37.197 dB. Our method that combines the CNN and Diffusion achieved consistently better results with PSNR = 38.920 dB than all the previous methods.

Table 2: Quantitative comparison of AC-SDPET generated from NAC-LDPET data. Best results are marked in **bold**..

Lesion	Error - SUV mean			
Quantification	5% Low-count	10% Low-count		
NAC-LD	0.1540 ± 0.0710	0.1517 ± 0.0740		
UNet Ronneberger et al. (2015b)	0.0989 ± 0.0394	0.0855 ± 0.0451		
cGAN Isola et al. (2017b)	0.0894 ± 0.0356	0.0805 ± 0.0393		
3D-DDPM Bieder et al. (2023)	0.0907 ± 0.0363	0.0874 ± 0.0368		
TPDM Lee et al. (2023)	0.0922 ± 0.0359	0.0911 ± 0.0399		
MADM	0.0787 ± 0.0391	0.0736 ± 0.0403		

The quantitative comparisons of local tumor regions were summarized in Table 2. Similar to the observa-

tions from the above global quality analysis, we found that NAC-LDPET suffers from significant lesion quantification errors thus resulting in an averaged SUV mean error over 0.15 in terms of RMSE under the 5% condition. Even though previous methods can significantly reduce lesion quantification errors, the performance reaches its limit at approximately 0.09. On the other hand, our MADM can further reduce this error to below 0.08 which significantly improves the lesion quantification.

3.1. Ablative Studies

Multi-view Averaging Strategies in MADM was studied and summarized in Table 3. Specifically, we investigated MADM's performance when different single view or combination of views strategies were implemented in MADM. As we can see, single-view strategies (first three rows) show consistently lower performance than the two-view combination strategies (fourth to seventh rows). MADM with all three views, i.e. axial, coronal, and sagittal, yields superior performance as compared to MADM with only one or two views.

Table 3: Ablative studies on the inclusion of multi-view averaging strategies in MADM.

and

means used and not used the model of the view in MADM, respectively, 5% NAC-LDPET is considered here.

RMSE
378 ± 0.0104
385 ± 0.0098
362 ± 0.0095
341 ± 0.0097
331 ± 0.0089
311 ± 0.0091
299 ± 0.0088

Multi-view Averaging vs Sequential-based Strategies was investigated and reported in Table 4. Specifically, we investigated a variant of MADM, called 2.5D Multi-View Sequential Diffusion (MVSD) that uses the same sets of 2.5D diffusion models as in MADM but was applied sequentially at multiple views during the sampling process. As we can see from the table, the MVSD approach, regardless of the order of axial, coronal, and sagittal views processed, exhibits negligible differences in performance, with PSNR values hovering around 38.61 dB and RMSE at approximately 0.0321. Our MADM on the last row achieved superior performance than all MVSD with different settings.

Table 4: Quantitative comparison of AC-SDPET generated from NAC-LDPET data. Best results are marked in **bold**. 5% NAC-LDPET is considered here.

2.5D Multi-View Sequential	PSNR	RMSE	
Axial → Coronal → Saggital	38.613 ± 1.500	0.0321 ± 0.0092	
Coronal → Saggital → Axial	38.609 ± 1.500	0.0321 ± 0.0092	
Saggital \rightarrow Axial \rightarrow Coronal	38.613 ± 1.499	0.0321 ± 0.0092	
MADM	38.920 ± 1.503	0.0299 ± 0.0088	

Table 5: Quantitative comparison of AC-SDPET generated from NAC-LDPET data. Best results are marked in **bold**. 5% NAC-LDPET is considered here.

Eval	PSNR	RMSE
2D MADM	37.816 ± 1.541	0.0386 ± 0.0110
2.5D MADM s = 4	38.759 ± 1.450	0.0309 ± 0.0080
2.5D MADM s = 8	38.920 ± 1.503	0.0299 ± 0.0088
2.5D MADM s = 12	38.772 ± 1.478	0.0309 ± 0.0087

Impact of 2.5D Setting in MADM was investigated and summarized in Table 5. As we can see, transitioning

from a 2D to a 2.5D in MADM elevates the PSNR from 37.82 dB to 38.92 dB and reduces the RMSE from 0.0386 to 0.0299. This enhancement in model performance is attributed to the 2.5D model's capability to integrate contextual information from adjacent slices. Figure 5 exemplifies that the 2.5D MADM more accurately predicts the shape and intensity in lesion areas (red arrows). By incorporating s upper and lower slices relative to the target slice into its input, the 2.5D model achieves a more comprehensive understanding and precise reconstruction of abnormal areas. We found that setting the number of adjacent slices to s = 8 yields the best performance, achieving a PSNR of 38.92 dB and an RMSE of 0.0299.

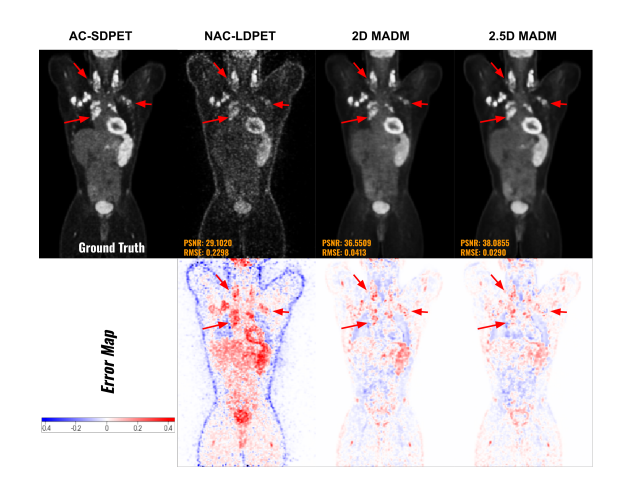


Figure 5: Visual comparison of AC-SDPET generation form 2D MADM and 2.5D MADM under 5% NAC-LDPET settings. The coronal view image(top) and error map(bottom) are shown. RMSE and PSNR values are calculated for each volume. The CT-based AC-SDPET(top) and image index into the color map of the error map(bottom) are shown in the first column.

Impact of CNN-Prior of MADM was investigated as well. A visual example is shown in Figure 7. As we can see, implementing a prior strategy within the MADM framework significantly enhances the accuracy of the translated 3D image and reduces the intensity errors here. In parallel, we also studied the impact of starting timestep t_s of using the prior image in the sampling process, and the results are summarized in Figure 6, where we plotted the translation's NMSE against t_s at an interval of 100. As we observe from this result, the NMSE first decreases as t_s increases. It reached the minimal NMSE

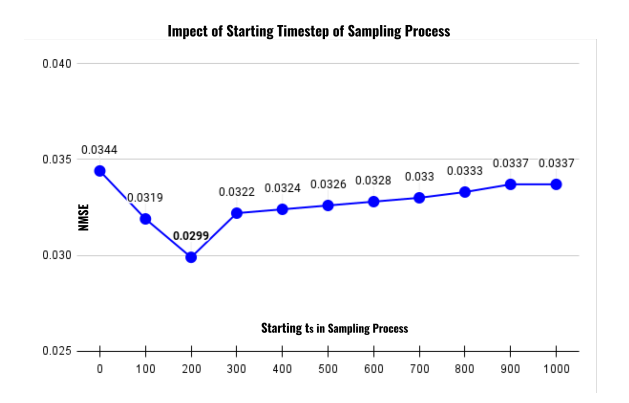


Figure 6: Ablative study on the starting time step of the diffusion sampling process. NMSE evaluation under the 5% NAC-LDPET setting is used here. Best performance is reached when $t_s = 200$.

of 0.0299 at $t_s = 200$ before the NMSE started to increase again. In contrast to previous diffusion methods that typically require $t_s = 1000$, our method with optimal performance at $t_s = 200$ outperforms them in terms of both speed and image quality. Please note that the result reported at $t_s = 0$ is c-GAN Isola et al. (2017b) without diffusion process.

4. Discussion

In this work, we develop a novel 3D image-toimage translation diffusion model, called 2.5D Multiview Averaging Diffusion Model (MADM), for reducing the radiation in PET acquisition by directly translating NAC-LDPET to AC-SDPET in 3D. During the training, MADM trains multiple lightweight 2.5D models from axial, coronal, and sagittal views. In parallel, a conventional 3D CNN-based network (i.e. 3D UNet here) is also trained. During the inference process, we first use the trained 3D UNet for generating a prior 3D image. Then, we utilize this 3D prior image with scheduled noise as a starting point in our diffusion process to further refine it. During the subsequent diffusion, all views' 2.5D models are applied in each sampling step and ensemble before proceeding to the next step. There are several key advantages of MADM. First, directly extending the previous 2D diffusion model into 3D is highly infeasible due to the challenge of large GPU memory requirements. MADM

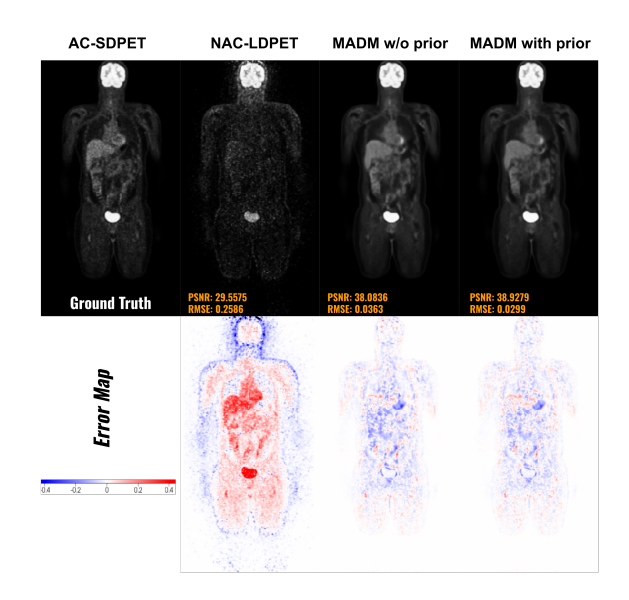


Figure 7: Visual comparison of AC-SDPET generation with and without UNet Prior in MADM. under 5% NAC-LDPET settings. The coronal view image(top) and error map(bottom) are shown. RMSE and PSNR values are calculated for each individual volume. The CT-based AC-SDPET(top) and image index in to the color map of the error map(bottom) are shown in the first column.

utilizes multiple lightweight 2.5D diffusion models instead of a 3D diffusion model, which makes it trainable on limited GPU memory settings, especially when dealing with high-resolution 3D image-to-image generation, e.g. NAC-LDPET to AC-SDPET 3D translation that explored in this work. As we can observe from the last two columns in Table 1, MADM training memory consumption (per batch) is nearly 10 times less than 3D-DDPM. Second, MADM uses two simple and efficient strategies to enable high-quality 3D translation. The first is to use a 2.5D model that can learn the translation with contextual information from adjacent slices. The second is to use 2.5D models from three different views, where we average their outputs during the sampling process to ensure the slice-by-slice inconsistencies are minimized thus improving the 3D translation. Third, training diffusion models often require large-scale datasets to achieve robust performance. In contrast to directly feeding limited amounts of whole 3D volumes into a 3D diffusion model for training, 2.5D inputs from multiple views extracted from 3D volumes naturally improve the number and diversity of the training data. In fact, as we can observe from Table 1 and Table 2, MADM achieved significantly better translation in terms of both global and local metrics, and we believe this is one of the main reasons. Lastly, we utilize the one-step inference 3D CNN model to generate a prior image as the starting point of the diffusion model, which not only reduces the number of required sampling steps but improves the translation accuracy.

However, our current work also has potential limitations, suggesting interesting directions for future studies. First, even though we reduce the memory requirement (Table 1) for diffusion-based 3D image-to-image translation, the inference speed of MADM per 3D volume in our applications takes about 10 minutes for the volume $192 \times 192 \times 192$ and up to 30 minutes for the volume 192×192×460 which one would consider long, especially when comparing with CNN-based methods. Depending on the user's time budget, MADM can adjust the starting time point of the diffusion process (Figure 6), trading the inference speed with the performance. As we can see from Figure 6, the optimal performance is achieved when $t_s = 200$. In this case, we can adjust the $t_s = 100$ to reduce the inference steps by two times, thus significantly reducing the inference time. While the performance reduces from NMSE of 0.0299 to 0.0319, the performance is still better than all the previous baselines in Table 1. In parallel, we can adjust the number of views of MADM to improve the inference speed. As we can see from Table 3, even though optimal performance was achieved when all three views were included, we can use the two-view setting, i.e. axial + saggital views, to reduce the inference time but still generate superior 3D translation performance as compared to previous baseline methods (Table 1). On the other hand, we could also replace the current 3D prior image generation network, i.e. 3D UNet, with more advanced network architecture, such as Transformer Vaswani et al. (2017); Dalmaz et al. (2022) and Multi-stage Network Zamir et al. (2021); Zhou et al. (2022a) to improve the prior 3D image generation, which may shorten the diffusion sampling process for optimal performance. Second, even though our results (Table 1) show that MADM achieved superior 3D translation performance as compared to previous state-of-the-art diffusion and CNN-based methods, one of the key limitations is that we don't know how confident we are with our translation. 3D pixel-wise uncertainty estimation is highly desirable. In fact, uncertainty estimation for the I2I diffusion model is already well-established in many previous works Zhou et al. (2024); Gong et al. (2024). In general, pixelwise uncertainty can be obtained by running the diffusion reverse pass multiple times and then computing the pixelwise standard deviation of the translated results. Similar here for MADM, we could also run multiple reverse passes by adding different noise to the same prior image, thus generating multiple 3D translation results. Then, the 3D pixel-wise uncertainty can be obtained by calculating the standard deviation of the translations. With the uncertainty map, one can identify areas where the model is confident and areas where it is not. One could use this information to fine-tune the model to reinforce the learning in the uncertain regions, thus potentially further improving the performance. In parallel to uncertainty estimation, averaging multiple runs' transition results as final translation also presents potential opportunities for further improving the performance Zhou et al. (2024). However, please note that utilizing this simple and efficient strategy for uncertainty estimation and performance gain comes at the cost of further elevated inference time, where the MADM inference time would increase linearly as the number of reverse runs increases. We recommend that users balance this trade-off in their application, especially in time-sensitive applications. Third, we only validated our 3D translation method for the application of PET dose reduction in this work. While we validate our method on clinically significant regions, i.e. tumors (Table 2), further analysis on the impacts on downstream analysis, such as prognosis and treatment planning, needs to be carried out in the future. In addition, interesting future directions also include validating MADM to other 3D medical imaging datasets and applications, such as 3D cross-modal MRI synthesis Li et al. (2023); Ji et al. (2022), 3D contrast image synthesis in CT/MRI Li et al. (2022); Choi et al. (2021); Liu et al. (2020b), Low-dose CT denoising Yin et al. (2019); Zhou et al. (2021, 2022a), and accelerated MRI reconstruction Zhou et al. (2023); Zhou and Zhou (2020); Zhou et al. (2022b). Finally, we would also like to add that - while we framed the MADM as an independent method for 3D translation here, we believe this 2.5Dbased method could be used for assisting the 3D networkbased diffusion translation once the computation barrier for it is not an issue in the future. Specifically, during the diffusion inference process, we could average the 3D results with the multi-view 2.5D results, and it could potentially further improve the translation performance. This is an interesting direction that we will investigate in our future works.

5. Conclusion

In this work, we developed a novel 2.5D Multi-view Averaging Diffusion Model (MADM) for 3D medical image translation with the first application on low-count PET reconstruction with CT-less AC. Our method has three key components. First, to reduce the computational demands associated with 3D models and to mitigate the discontinuities inherent in 2D models, we proposed to use a 2.5D model that incorporates several adjacent slices in addition to the target slice for prediction. Second, to further minimize discontinuities and enhance prediction accuracy, we proposed to train separate 2.5D models for each view in 3D. During the inference, we average the result in each denoising step of the diffusion process. Third, to accelerate the translation process and refine generated image accuracy, we proposed to utilize 3D predictions from a CNN-based model as a prior for our diffusion model. Our experimental results show that MADM can generate high-quality AC standard-count PET(AC-SDPET) directly from the NAC low-count PET(NAC-LDPET) with limited computation memory resources, and outperforming several previous baselines. We believe our method can be extended to other 3D imaging applications, and potentially useful in other clinical applications.

Acknowledgments

This work was supported by the National Institutes of Health (NIH) grant R01EB025468, grant R01CA275188, and Yale PhD fellowship.

Declaration of Competing Interest

The authors declare that they have no known competing financial interests or personal relationships that could have appeared to influence the work reported in this paper.

Credit authorship contribution statement

Yinchi Zhou: Conceptualization, Methodology, Software, Visualization, Validation, Formal analysis, Writing original draft. Tianqi Chen: Results analysis, Writing - review and editing. Jun Hou: Results analysis, Writing - review and editing. Huidong Xie: Conceptualization, Methodology, Software, Writing - review and editing. Nicha C. Dvornek: Writing - review and editing. S. Kevin Zhou: Data preparation, Writing - review and editing. David L. Wilson: Data preparation, Writing - review and editing Chi Liu: Writing - review and editing Bo Zhou: Conceptualization, Methodology, Software, Visualization, Validation, Formal analysis, Writing original draft, Supervision.

References

Arjovsky, M., Chintala, S., Bottou, L., 2017. Wasserstein gan. arXiv preprint arXiv:1701.07875.

Bieder, F., Wolleb, J., Durrer, A., Sandkühler, R., Cattin, P.C., 2023. Diffusion models for memory-efficient processing of 3d medical images. arXiv preprint arXiv:2303.15288.

Chen, K.T., Gong, E., de Carvalho Macruz, F.B., Xu, J., Boumis, A., Khalighi, M., Poston, K.L., Sha, S.J., Greicius, M.D., Mormino, E., et al., 2019. Ultra-low-dose 18f-florbetaben amyloid pet imaging using deep learning with multi-contrast mri inputs. Radiology 290, 649–656.

Chen, X., Liu, C., 2023. Deep-learning-based methods of attenuation correction for spect and pet. Journal of Nuclear Cardiology 30, 1859–1878.

Choi, J.W., Cho, Y.J., Ha, J.Y., Lee, S.B., Lee, S., Choi, Y.H., Cheon, J.E., Kim, W.S., 2021. Generating synthetic contrast enhancement from non-contrast chest computed tomography using a generative adversarial network. Scientific reports 11, 20403.

Chung, H., Ryu, D., McCann, M.T., Klasky, M.L., Ye, J.C., 2023. Solving 3d inverse problems using pretrained 2d diffusion models, in: Proceedings of the

- IEEE/CVF Conference on Computer Vision and Pattern Recognition (CVPR), pp. 22542–22551.
- Dalmaz, O., Yurt, M., Çukur, T., 2022. Resvit: residual vision transformers for multimodal medical image synthesis. IEEE Transactions on Medical Imaging 41, 2598–2614.
- Dong, X., Lei, Y., Wang, T., Higgins, K., Liu, T., Curran, W.J., Mao, H., Nye, J.A., Yang, X., 2020. Deep learning-based attenuation correction in the absence of structural information for whole-body positron emission tomography imaging. Physics in Medicine & Biology 65, 055011.
- Dong, X., Wang, T., Lei, Y., Higgins, K., Liu, T., Curran, W.J., Mao, H., Nye, J.A., Yang, X., 2019. Synthetic ct generation from non-attenuation corrected pet images for whole-body pet imaging. Physics in Medicine & Biology 64, 215016.
- Dutta, J., Leahy, R.M., Li, Q., 2013. Non-local means denoising of dynamic pet images. PloS one 8, e81390.
- Gong, K., Johnson, K., El Fakhri, G., Li, Q., Pan, T., 2024. Pet image denoising based on denoising diffusion probabilistic model. European Journal of Nuclear Medicine and Molecular Imaging 51, 358–368.
- Gong, Y., Shan, H., Teng, Y., Tu, N., Li, M., Liang, G., Wang, G., Wang, S., 2020. Parameter-transferred wasserstein generative adversarial network (pt-wgan) for low-dose pet image denoising. IEEE Transactions on Radiation and Plasma Medical Sciences.
- Goodfellow, I., Pouget-Abadie, J., Mirza, M., Xu, B., Warde-Farley, D., Ozair, S., Courville, A., Bengio, Y., 2014. Generative adversarial nets, in: Advances in neural information processing systems, pp. 2672–2680.
- Hu, Z., Xue, H., Zhang, Q., Gao, J., Zhang, N., Zou, S.,
 Teng, Y., Liu, X., Yang, Y., Liang, D., et al., 2020.
 Dpir-net: Direct pet image reconstruction based on the wasserstein generative adversarial network. IEEE Transactions on Radiation and Plasma Medical Sciences.
- Hwang, D., Kang, S.K., Kim, K.Y., Seo, S., Paeng, J.C., Lee, D.S., Lee, J.S., 2019. Generation of pet attenuation map for whole-body time-of-flight 18f-fdg

- pet/mri using a deep neural network trained with simultaneously reconstructed activity and attenuation maps. Journal of Nuclear Medicine 60, 1183–1189.
- Isola, P., Zhu, J.Y., Zhou, T., Efros, A.A., 2017a. Imageto-image translation with conditional adversarial networks, in: Proceedings of the IEEE conference on computer vision and pattern recognition, pp. 1125–1134.
- Isola, P., Zhu, J.Y., Zhou, T., Efros, A.A., 2017b. Imageto-image translation with conditional adversarial networks, in: Proceedings of the IEEE Conference on Computer Vision and Pattern Recognition (CVPR).
- Ji, S., Yang, D., Lee, J., Choi, S.H., Kim, H., Kang, K.M., 2022. Synthetic mri: technologies and applications in neuroradiology. Journal of Magnetic Resonance Imaging 55, 1013–1025.
- Kaplan, S., Zhu, Y.M., 2019. Full-dose pet image estimation from low-dose pet image using deep learning: a pilot study. Journal of digital imaging 32, 773–778.
- Lee, J.S., 2020. A review of deep-learning-based approaches for attenuation correction in positron emission tomography. IEEE Transactions on Radiation and Plasma Medical Sciences 5, 160–184.
- Lee, S., Chung, H., Park, M., Park, J., Ryu, W.S., Ye, J.C., 2023. Improving 3d imaging with pre-trained perpendicular 2d diffusion models, in: Proceedings of the IEEE/CVF International Conference on Computer Vision, pp. 10710–10720.
- Li, H.B., Conte, G.M., Anwar, S.M., Kofler, F., Ezhov, I., van Leemput, K., Piraud, M., Diaz, M., Cole, B., Calabrese, E., et al., 2023. The brain tumor segmentation (brats) challenge 2023: Brain mr image synthesis for tumor segmentation (brasyn). ArXiv.
- Li, W., Lam, S., Li, T., Cheung, A.L.Y., Xiao, H., Liu, C., Zhang, J., Teng, X., Zhi, S., Ren, G., et al., 2022. Multi-institutional investigation of model generalizability for virtual contrast-enhanced mri synthesis, in: International Conference on Medical Image Computing and Computer-Assisted Intervention, Springer. pp. 765–773.

- Liu, F., Jang, H., Kijowski, R., Bradshaw, T., McMillan, A.B., 2018a. Deep learning mr imaging-based attenuation correction for pet/mr imaging. Radiology 286, 676–684.
- Liu, F., Jang, H., Kijowski, R., Zhao, G., Bradshaw, T., McMillan, A.B., 2018b. A deep learning approach for 18f-fdg pet attenuation correction. EJNMMI physics 5, 1–15
- Liu, H., Wu, J., Lu, W., Onofrey, J.A., Liu, Y.H., Liu, C., 2020a. Noise reduction with cross-tracer and cross-protocol deep transfer learning for low-dose pet. Physics in Medicine & Biology 65, 185006.
- Liu, J., Tian, Y., Ağıldere, A.M., Haberal, K.M., Coşkun, M., Duzgol, C., Akin, O., 2020b. Dyefreenet: Deep virtual contrast ct synthesis, in: Simulation and Synthesis in Medical Imaging: 5th International Workshop, SASHIMI 2020, Held in Conjunction with MICCAI 2020, Lima, Peru, October 4, 2020, Proceedings 5, Springer. pp. 80–89.
- Lu, W., Onofrey, J.A., Lu, Y., Shi, L., Ma, T., Liu, Y., Liu, C., 2019. An investigation of quantitative accuracy for deep learning based denoising in oncological pet. Physics in Medicine & Biology 64, 165019.
- Maggioni, M., Katkovnik, V., Egiazarian, K., Foi, A., 2012. Nonlocal transform-domain filter for volumetric data denoising and reconstruction. IEEE transactions on image processing 22, 119–133.
- Mejia, J., Mederos, B., Mollineda, R.A., Maynez, L.O., 2016. Noise reduction in small animal pet images using a variational non-convex functional. IEEE Transactions on Nuclear Science 63, 2577–2585.
- Nuyts, J., Rezaei, A., Defrise, M., 2018. The validation problem of joint emission/transmission reconstruction from tof-pet projections. IEEE Transactions on Radiation and Plasma Medical Sciences 2, 273–278.
- Ouyang, J., Chen, K.T., Gong, E., Pauly, J., Zaharchuk, G., 2019. Ultra-low-dose pet reconstruction using generative adversarial network with feature matching and task-specific perceptual loss. Medical physics 46, 3555–3564.

- Pan, S., Abouei, E., Peng, J., Qian, J., Wynne, J.F., Wang, T., Chang, C.W., Roper, J., Nye, J.A., Mao, H., et al., 2024. Full-dose whole-body pet synthesis from low-dose pet using high-efficiency denoising diffusion probabilistic model: Pet consistency model. Medical Physics.
- Rezaei, A., Michel, C., Casey, M.E., Nuyts, J., 2016. Simultaneous reconstruction of the activity image and registration of the ct image in tof-pet. Physics in Medicine & Biology 61, 1852.
- Ronneberger, O., Fischer, P., Brox, T., 2015a. Unet: Convolutional networks for biomedical image segmentation, in: International Conference on Medical image computing and computer-assisted intervention, Springer. pp. 234–241.
- Ronneberger, O., Fischer, P., Brox, T., 2015b. Unet: Convolutional networks for biomedical image segmentation, in: Navab, N., Hornegger, J., Wells, W.M., Frangi, A.F. (Eds.), Medical Image Computing and Computer-Assisted Intervention MICCAI 2015, Springer International Publishing, Cham. pp. 234–241.
- Shi, L., Zhang, J., Toyonaga, T., Shao, D., Onofrey, J.A., Lu, Y., 2023. Deep learning-based attenuation map generation with simultaneously reconstructed pet activity and attenuation and low-dose application. Physics in Medicine & Biology 68, 035014.
- Shiri, I., Ghafarian, P., Geramifar, P., Leung, K.H.Y., Ghelichoghli, M., Oveisi, M., Rahmim, A., Ay, M.R., 2019.
 Direct attenuation correction of brain pet images using only emission data via a deep convolutional encoderdecoder (deep-dac). European radiology 29, 6867–6879.
- Shiri, I., Salimi, Y., Maghsudi, M., Jenabi, E., Harsini, S., Razeghi, B., Mostafaei, S., Hajianfar, G., Sanaat, A., Jafari, E., et al., 2023. Differential privacy preserved federated transfer learning for multi-institutional 68gapet image artefact detection and disentanglement. European journal of nuclear medicine and molecular imaging, 1–14.
- Strauss, K.J., Kaste, S.C., 2006. The alara (as low as reasonably achievable) concept in pediatric interventional

- and fluoroscopic imaging: striving to keep radiation doses as low as possible during fluoroscopy of pediatric patients—a white paper executive summary. Radiology 240, 621–622.
- Toyonaga, T., Shao, D., Shi, L., Zhang, J., Revilla, E.M., Menard, D., Ankrah, J., Hirata, K., Chen, M.K., Onofrey, J.A., et al., 2022. Deep learning–based attenuation correction for whole-body pet—a multitracer study with 18f-fdg, 68 ga-dotatate, and 18f-fluciclovine. European Journal of Nuclear Medicine and Molecular Imaging 49, 3086–3097.
- Vaswani, A., Shazeer, N., Parmar, N., Uszkoreit, J., Jones, L., Gomez, A.N., Kaiser, Ł., Polosukhin, I., 2017. Attention is all you need. Advances in neural information processing systems 30.
- Wang, Y., Yu, B., Wang, L., Zu, C., Lalush, D.S., Lin, W., Wu, X., Zhou, J., Shen, D., Zhou, L., 2018. 3d conditional generative adversarial networks for high-quality pet image estimation at low dose. Neuroimage 174, 550–562.
- Xiang, L., Qiao, Y., Nie, D., An, L., Lin, W., Wang, Q., Shen, D., 2017. Deep auto-context convolutional neural networks for standard-dose pet image estimation from low-dose pet/mri. Neurocomputing 267, 406–416.
- Xie, H., Gan, W., Zhou, B., Chen, X., Liu, Q., Guo, X., Guo, L., An, H., Kamilov, U.S., Wang, G., Liu, C., 2023. DDPET-3D: Dose-aware Diffusion Model for 3D Ultra Low-dose PET Imaging. URL: http://arxiv.org/abs/2311.04248, doi:10.48550/arXiv.2311.04248. arXiv:2311.04248 [eess].
- Yin, X., Zhao, Q., Liu, J., Yang, W., Yang, J., Quan, G., Chen, Y., Shu, H., Luo, L., Coatrieux, J.L., 2019. Domain progressive 3d residual convolution network to improve low-dose ct imaging. IEEE transactions on medical imaging 38, 2903–2913.
- Zamir, S.W., Arora, A., Khan, S., Hayat, M., Khan, F.S., Yang, M.H., Shao, L., 2021. Multi-stage progressive image restoration, in: Proceedings of the IEEE/CVF Conference on Computer Vision and Pattern Recognition, pp. 14821–14831.

- Zhou, B., Chen, X., Xie, H., Zhou, S.K., Duncan, J.S., Liu, C., 2022a. Dudoufnet: Dual-domain under-tofully-complete progressive restoration network for simultaneous metal artifact reduction and low-dose ct reconstruction. IEEE Transactions on Medical Imaging 41, 3587–3599.
- Zhou, B., Chen, X., Zhou, S.K., Duncan, J.S., Liu, C., 2021. Dudodr-net: Dual-domain data consistent recurrent network for simultaneous sparse view and metal artifact reduction in computed tomography. Medical Image Analysis, 102289.
- Zhou, B., Schlemper, J., Dey, N., Salehi, S.S.M., Liu, C., Duncan, J.S., Sofka, M., 2022b. Dsformer: A dual-domain self-supervised transformer for accelerated multi-contrast mri reconstruction. arXiv preprint arXiv:2201.10776.
- Zhou, B., Zhou, S.K., 2020. Dudornet: Learning a dual-domain recurrent network for fast mri reconstruction with deep t1 prior, in: Proceedings of the IEEE conference on computer vision and pattern recognition, pp. 298–313.
- Zhou, L., Schaefferkoetter, J.D., Tham, I.W., Huang, G., Yan, J., 2020. Supervised learning with cyclegan for low-dose fdg pet image denoising. Medical Image Analysis 65, 101770.
- Zhou, Y., Chen, T., Hou, J., Xie, H., Dvornek, N.C., Zhou, S.K., Wilson, D.L., Duncan, J.S., Liu, C., Zhou, B., 2024. Cascaded multi-path shortcut diffusion model for medical image translation. arXiv preprint arXiv:2405.12223.
- Zhou, Y., Wang, H., Liu, C., Liao, B., Li, Y., Zhu, Y., Hu, Z., Liao, J., Liang, D., 2023. Recent advances in highly accelerated 3d mri. Physics in Medicine & Biology 68, 14TR01.
- Zhu, J.Y., Park, T., Isola, P., Efros, A.A., 2017. Unpaired image-to-image translation using cycle-consistent adversarial networks, in: Proceedings of the IEEE International Conference on Computer Vision, pp. 2223– 2232.